Journal of Biotechnology 407 (2025) 12–21

Contents lists available at ScienceDirect

Journal of Biotechnology

journal homepage: www.elsevier.com/locate/jbiotec

Channel matters: Overcoming diffusion bottlenecks via loop engineering of LinD for enhanced isoprene production

Julian L. Wissner [a,1], Max-Philipp Fischer [b,1], Wendy Escobedo-Hinojosa [b,c,1], Jan Klenk [b], Bettina M. Nestl [b], Jan Seeger [b], Anibal Cuetos [d], Gideon Grogan [d], Javier Iglesias-Fernández [e], Sílvia Osuna [e,f], Gloria Saab-Rincón [a], Bernhard Hauer [b,*]

[a] Departamento de Ingeniería Celular y Biocatálisis, Instituto de Biotecnología, Universidad Nacional Autónoma de México, Avenida Universidad 2001, Colonia Chamilpa, Morelos, Cuernavaca 62210, Mexico
[b] Institute of Technical Biochemistry, University of Stuttgart, Allmandring 31, Stuttgart 70569, Germany
[c] Unidad de Química en Sisal, Facultad de Química, Universidad Nacional Autónoma de México, Puerto de abrigo s/n, Yucatán, Sisal 97356, Mexico
[d] Department of Chemistry, York Structural Biology Laboratory, University of York, York YO10 5DD, United Kingdom
[e] Departament de Química, CompBioLab group, Institut de Química Computacional i Catàlisi, Carrer Maria Aurèlia Capmany 69, Girona 17003, Spain
[f] ICREA, Pg. Lluís Companys 23, Barcelona 08010, Spain

ARTICLE INFO

Keywords:
Linalool dehydratase isomerase (LinD)
C-C activation
Protein channels
Enzyme engineering
Isoprene

ABSTRACT

The selective chemical dehydration leading to C═C double bond formation is a challenging reaction that harbors great potential for industrial applications. The cofactor independent bifunctional linalool dehydratase isomerase (LinD) from *Castellaniella defragrans* catalyzes the reversible dehydration of (*S*)-linalool to myrcene, as well as its isomerization to geraniol. We previously reported that LinD is able to convert the small alkenol 2-methyl-3-buten-2-ol to the valuable product isoprene. To foster the LinD-catalyzed production of isoprene in a novel recombinant *E. coli* whole-cell two-phase system, we targeted the active site and a flexible α-helix near the putative substrate channel via enzyme engineering. Interestingly, none of the active site variants exhibited an increased product formation. In contrast, saturation mutagenesis of the 10 amino acids forming the α-helix, identified the variants K103N, R104G, G107T and D112T, which exhibited a 1.73 ± 0.05, 1.56 ± 0.12, 2.08 ± 0.12 and 1.93 ± 0.06-fold increase in product formation compared to the wild-type enzyme, respectively. Notably, a combinatorial approach targeting these four variants led to decreased activity in all cases, compared to the corresponding single-point variants, indicating negative epistatic interactions. Thus, employing the most catalytically efficient single point variant G107T, which exhibited a 28-fold higher $k_{cat\ (app)}$ compared to the wild-type, a total of 2.8 ± 0.2 mM isoprene was obtained utilizing the whole-cell two-phase system. Crystallographic analysis of G107T revealed only minor structural changes; however, molecular dynamic simulations uncovered striking conformational differences relative to the LinD wild-type, emphasizing the role of altered substrate channel in variant G107T.

1. Introduction

The selective hydration or dehydration of water at non-activated C═C double bonds is a highly sought-after reaction in synthetic organic chemistry. Chemically, this reaction is challenging to achieve selectively and is often accompanied by undesired side reactions and extreme reaction conditions, such as high temperatures and pressures, or the use of strong acids, are limiting factors (Frija and Afonso, 2012; Raju et al., 2015; Resch and Hanefeld, 2015; Zhang et al., 2016). Thus, an enzyme-catalyzed approach for the selective addition or elimination of water is advantageous, since enzymatic reactions typically function under mild conditions in aqueous solutions and often exhibit higher selectivity than chemical synthesis (Nestl et al., 2011; Shoda et al., 2016). (De)hydratases catalyze the (de)hydration of isolated as well as conjugated C═C double bonds, with the former following the Markovnikov Rule (Demming et al., 2018; Isenberg and Grdinic, 1969).

* Corresponding author.
E-mail address: bernhard.hauer@itb.uni-stuttgart.de (B. Hauer).
[1] These authors contributed equally to this work.

https://doi.org/10.1016/j.jbiotec.2025.07.019
Received 19 May 2025; Received in revised form 18 July 2025; Accepted 21 July 2025
Available online 25 July 2025

Naturally, (de)hydratases are widespread enzymes and occur for example in mitochondria of yeast (Kastaniotis et al., 2004) or in rat liver peroxisomes (Li et al., 1990). Since the 1970s, natural dehydration machinery of microorganisms, such as yeast or Brevibacteria, have been used for instance, for the production of maleic acid from fumarate (Neufeld et al., 1991; Yamamoto et al., 1976). However, heretofore, heterologous expressed (de)hydratases are scarcely used for industrial application, despite harboring great potential. One example is oleate hydratase 1 from *Elizabethkingia meningoseptica* (EmOAH1), which was recently reported to accept not only terminal long-chained alkenes (Demming et al., 2017, 2019), but also terminal small-chained alkenes (Härterich et al., 2025) for hydration, giving access to valuable optically active secondary alcohols. Likewise, the enzyme was shown to accept not only fatty acids, but also fatty alcohols, fatty amines, and other altered substrates (Engleder, Strohmeier, et al., 2019). Another (de) hydratase with great potential is the bifunctional linalool dehydratase isomerase (LinD) from *Castellaniella defragrans*, which was described first in 2010 by Brodkorb and co-workers and is considered to be involved in the degradation of monoterpenes (Brodkorb et al., 2010). In *C. defragrans*, LinD catalyzes the isomerization of geraniol **1** to (*S*)-linalool **2** as well as its reversible dehydration to myrcene **3** (Fig. 1 A), a dual activity from which the enzyme derives its name. Notably, LinD is a cofactor-free enzyme, and its reactions proceed via an acid/-base mechanism involving protonable amino acid side chains (Nestl et al., 2017; Weidenweber et al., 2016). Additionally, LinD was shown to accept much shorter substrates than previously anticipated (Nestl et al., 2017). The shortest accepted tertiary alcohol is 2-methyl-3-buten-2-ol **4**, which LinD dehydrates to the valuable compound isoprene **5** (Fig. 1 B), a volatile C5 hydrocarbon which serves as crucial building block for synthetic rubber and various natural products (Isar et al., 2022). Industrially, **5** is produced by petrochemical routes (Taalman, 1996), such as a byproduct of ethylene production via steam cracking (Chauvel and Lefebvre, 1989). However, due to the environmental concerns associated with steam cracking, there has been increasing interest in biotechnological alternatives to decouple **5** production from petroleum-based resources.

The present study aimed to enhance the LinD catalyzed production of **5** in a recombinant *E. coli* whole-cell system through enzyme engineering. Therefore, two promising regions were targeted, the active site, as well as a short and flexible α-helix close to the putative substrate channel (Weidenweber et al., 2016), determined via B-factor analysis (Sun et al., 2019) of the LinD crystal structure (PDB: 5G1W). Kinetic investigations of the four LinD variants producing the highest isoprene concentration were conducted using the whole-cell system. Molecular dynamics simulations of these variants, combined with the crystallized structure of the most promising variant, G107T, highlighted their role in substrate diffusion, ultimately enhancing enzymatic activity.

2. Material and methods

2.1. Construction of expression plasmids

The gene encoding LinD was purchased codon optimized for expression in *E. coli* (Geneart AG, Regensburg, Germany) and subcloned into the vector pET-28a(+) (SI chapter 1 for detailed information). To enhance periplasmic accumulation of LinD in recombinant *E. coli*, its natural N-terminal tag was replaced with the OmpA signal sequence (Engleder, Müller, et al., 2019; Humphreys et al., 2000; Makrides, 1996), resulting in the fusion protein OmpA-LinD (OL). Therefore, the LinD encoding gene was amplified and the OmpA-tag was introduced via overlapping PCR, resulting in the construct pET-28a(+)::OmpA-LinD. This construct as well as the pET-28a(+) empty vector were used as templates for PCR for amplification of fragments for Gibson Assembly (Gibson et al., 2009). To assess the level of expression of LinD and its variants in cell lysates, monomeric red fluorescent protein-1 (mRFP1) was utilized (Campbell et al., 2002). The OmpA-LinD-mRFP1 fusion protein (OLm) was generated by insertion the codon-optimized *mRFP1* gene (Geneart AG; Regensburg, Germany) via Gibson Assembly, yielding the construct pET-28a(+)::OmpA-LinD-mRFP1. Therefore, a 4-amino-acid linker (Leu-Ala-Leu-Glu) was C-terminally fused to LinD by overlapping PCR during amplification of fragments for Gibson Assembly. All generated plasmids were transformed into *E. coli* XL-1 Blue. Plasmid DNA was validated by Sanger sequencing (Eurofins Genomic Germany GmbH; Ebersberg, Germany).

2.2. Expression of LinD encoding genes

Plasmids encoding LinD, OL and OLm, were used to transform *E. coli* JM83(DE3) (Kunkel, 1985). Precultures were inoculated with a single colony in 5 mL of LB medium supplemented with kanamycin. Main cultures in 4 mL of TB medium were inoculated with 1 % (v/v) precultures in 24-deep-well plates and incubated at 37°C and 180 rpm for 4 h. Expression was then induced with 1 mM IPTG, followed by incubation at 20°C and 180 rpm for 18 h. Cells were harvested by centrifugation at 2000 rcf for 20 min at 4°C, resuspended in 3 mL of reaction buffer (100 mM NaPi, 2 % (w/v) D-sorbitol, pH 6), and stored at 4°C until further use.

2.3. Construction of OmpA-LinD-mRFP1 variants

2.3.1. QuikChange mutagenesis

For the generation of single-point variants through QuikChange™, the plasmid pET-28a(+)::OmpA-LinD-mRFP1 was used as a template, and mutagenic oligonucleotides were designed and incorporated into a standard reaction mixture with KOD Hot Start DNA Polymerase

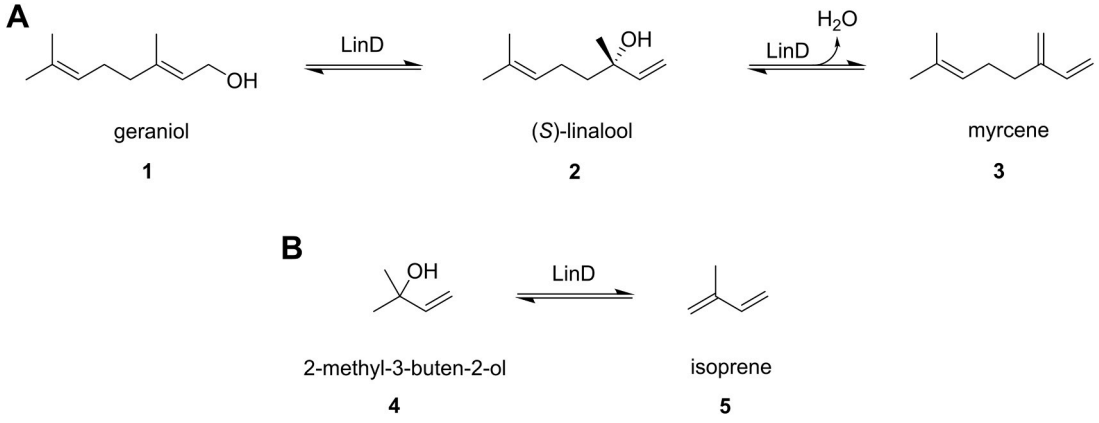

Fig. 1. A: Native LinD catalyzed isomerization of geraniol 1 to (*S*)-linalool 2 and reversible dehydration of 2 to myrcene 3. B: Promiscuous LinD catalyzed dehydration of 2-methyl-3-buten-2-ol 4 to isoprene 5.

(Novagen®; Darmstadt, Germany) (SI chapter 1). After amplification, 30 U *Dpn*I (New England BioLabs® GmbH; Ipswich, Massachusetts, USA) was added and incubated for 2 h at 37°C to digest methylated template DNA in the PCR products. After inactivation of *Dpn*I for 20 min at 65 °C, the PCR reaction mixture was cleaned by Zyppy DNA Clean and Concentrator Kit following the manufacturer's instructions. Clean DNA was used to transform *E. coli* XL-1 Blue.

2.3.2. Mutagenesis via overlap extension PCR

Using overlapping extension PCR (Kunkel, 1985), two partially complementary oligonucleotides were designed exhibiting an overlap at the 5'-end with a melting temperature > 55 °C, and at least 20 bp in length (SI chapter 1). The complementary region terminated immediately before the target codon on the leading strand. The forward oligonucleotide contained the desired mutation, while the reverse oligonucleotide remained unaltered. The non-complementary 3'-ends were designed with a melting temperature of approximately 60°C. After amplification, the PCR product was purified as described above and used to transform *E. coli* XL-1 Blue. Successful integration was confirmed by Sanger sequencing (Eurofins genomics; Ebersberg, Germany), after which the plasmid DNA was used to transform *E. coli* JM83(DE3) for expression. For site-saturation mutagenesis, overlap extension PCR was used in combination with the '22c trick' (Kille et al., 2013). Combination variants were generated either by QuikChange or overlap extension PCR.

2.4. Quantification of LinD expression levels

Fluorescence analysis of OLm fusion protein and controls was performed after chemical cell lysis. 150 µL of 1x BugBuster® was added to 150 µL cell culture in 96 microtiter plates and incubated for 10 min at 300 rpm and RT. Afterwards, insoluble cell debris was pelleted by centrifugation at 4000 rcf, for 20 min, at 4 °C. Then, 100 µL of the supernatant was transferred into a new 96 well plate. Fluorescence was measured using a POLARstar Omega (BMG Labtech GmbH; Ortenberg, Germany). Excitation was performed at 575 nm and fluorescence measured at 610 nm as endpoint measurements with constant gain of 2200 (filters: Ser.-Nr. 415–1499, 575–10 und 610–10; BMG Labtech GmbH; Ortenberg, Germany). Fluorescence data were used to determine the OLm protein content by referencing a calibration curve of IMAC-purified, lyophilized mRFP1-His6 and normalizing for molecular mass.

2.5. Initial biotransformations with cell lysate

Cell disruption was performed by ultrasonication after adding 0.1 % (v/v) of 100 mM PMSF stock solution (dissolved in ethanol) to inhibit endogenous proteases. Samples were pre-cooled in an ice bath and sonicated for 5 min using an output setting of 4 and a duty cycle of 35 %, while maintaining the samples on ice throughout the procedure. The resulting crude extract was centrifuged at 21,000 × g for 20 min at 4 °C to pellet the insoluble cell debris. The supernatant was collected and sterile-filtered using 0.2 µm filters and used immediately.

2.6. Biotransformations in a whole-cell-based two-phase system

To minimize the evaporation of product **5** during the biotransformation of **4**, an optimized two-phase system was developed. Therefore, all biotransformations were carried out in GC vials, where 850 µL of recombinant *E. coli* whole-cell suspension was transferred. After addition of 100 µL DTT solution (20 mM in reaction buffer), 900 µL cyclohexane was added as second phase. Reactions were initiated by addition of 50 µL substrate stock in DMSO and the vials immediately capped. Unless otherwise specified, the total substrate concentration in the aqueous phase was set to 10 mM. Samples were incubated for 18 h at 30 °C and 180 rpm. This system eliminated the need for sample extraction, as 1 µL of the cyclohexane phase could be directly injected into the GC/MS for analysis.

2.7. Analytics

Quantitative measurements of substrates and products was performed using a GC/MS QP2010 (Shimadzu Crop.; Kyoto, Japan) equipped with a PAL AOC-5000 Auto Injector (Shimadzu Corp.; Kyoto, Japan) and a Zebron ZB-5MSi capillary column (Art. No. 7HG-G018–11 (5 %-Phenyl-)methyl- 95 %-dimethylpolysiloxane, length 30 m, diameter 0.25 mm; film thickness 0.25 µm; Phenomenex Inc.; Torrance, CA, USA). Helium was used as carrier gas at a constant pressure of 26.7 kPa. 1 µL of the organic phase of the described two-phase system was injected at 250 °C, while split ratio was always kept at 50. For all analytes, short isothermal methods were used. Racemic model substrate **2** and its product **3** were analyzed at 160 °C for 4.5 min, with detection in SCAN mode using an *m/z* range of 15–160. Their retention times were 3.07 min for **2** and 2.71 min for **3**. Compounds **4** and **5** were analyzed at 70 °C for 2.6 min, with detection in SIM mode using *m/z* 67 and 71. Their retention times were 2.29 min for **4** and 2.05 min for **5** (Fig. S1).

2.8. Crystal structure of LinD G107T

2.8.1. Expression and purification of LinD G107T

The pET-28a(+)::OmpA-LinD-mRFP1-G107T plasmid was used to transform *E. coli* BL21(DE3) cells and glycerol stocks were prepared. For the preparation of the G107T mutant, an individual glycerol stock was used to inoculate a 5 mL LB medium pre-culture containing 30 µg mL^{-1} kanamycin, which was then incubated overnight at 37 °C with shaking at 180 rpm. These cultures were used to inoculate 1 L of TB medium and 30 µg mL^{-1} kanamycin in 2 L Erlenmeyer flasks. Cells were grown at 37 °C and 180 rpm, until an OD_{600} of 1.7–2 was reached, at which point 1 mM IPTG was added to induce gene expression. Cultures were then incubated overnight at 16 °C while shaking at 180 rpm. Cells were harvested by centrifugation at 4000 x *g* for 20 min at 4 °C. Pelleted cells were resuspended in 80 mM Tris·HCl buffer pH 8.0 also containing 500 mM NaCl, 2 % w/w sorbitol and 20 mM imidazole and the suspensions were then ultrasonicated at 14,000 microns (25 s on x 35 s off) for 5 cycles. The resulting suspensions were then centrifuged at 16,000 x *g* for 40 min at 4 °C. The recovered supernatant was loaded onto a 5 mL HisTrap FF crude column charged with 0.1 M nickel sulfate. The LinD G107T mutein was eluted using a 20–500 mM imidazole gradient over 15 column volumes. The pooled peak fractions were concentrated, loaded onto a HiLoad 16/600 Superdex 200 prep grade (GE Healthcare) gel filtration column and eluted with a buffer containing 80 mM Tris·HCl buffer at pH 8.0 with 500 mM NaCl and 2 % w/w sorbitol. Finally, the fractions were pooled, concentrated, and stored at 4 °C for subsequent experiments.

2.8.2. Protein crystallization

The LinD G107T mutant was concentrated to 10 mg mL^{-1} using a Vivaspin centricon with a 30 kDa molecular weight cut-off membrane. The concentrated protein was incubated with 3 mM DTT and 5 mM **4** prior to deposition into 96-well plates containing commercial crystallization screens by a Mosquito robot (TTP Lab Technologies). Crystal drops contained 150 nL each of the protein and reservoir solutions. The best hit for the mutant was optimized and scaled up into either 48-well plates in sitting-drop format, again using a Mosquito robot with 300 nL each of protein solution and reservoir, or into 24-well plate Linbro dishes using the hanging drop technique, where the volume of the reservoir was 1 mL and the crystal drops contained 1 µL each of protein solution and the reservoir. Optimized crystallization conditions for LinD G107T were 5 mg mL^{-1} protein concentration, 0.2 M sodium malonate, 0.1 M Bis-Tris propane pH 6.0, 20 % w/w PEG 3350 and 3 % v/v 2-methyl-2,4-pentanediol (MPD). The collection and processing of crystallographic data is described in the supplementary information in detail (SI chapter 4).

2.9. Computational methods, kinetics analysis, and macro- and microscopic analysis

Related information is provided in detail in the supplementary material (SI chapter 5, chapter 6 and chapter 7, respectively).

3. Results and discussion

3.1. Gene expression and biotransformation set-up

Biotransformations involving volatile compounds present challenges due to the loss of substrate and product during sample work-up. To address this, a two-phase system was developed for the biotransformation of substrate **4** and its dehydration product **5**, both of which are highly volatile. This system allows for the direct injection of the organic second phase (cyclohexane) into GC/MS, minimizing material loss due to evaporation in the downstream sample preparation. Additionally, it streamlines the process and supports medium-throughput screening by shortening the GC/MS analysis time. Due to the poor solvent stability of LinD, lysates of heterologously expressed LinD did not exhibit any activity when overlaid with cyclohexane as the second phase (data not shown). Therefore, recombinant *E. coli* JM83(DE3) whole-cells were utilized, if not stated otherwise.

LinD naturally contains an N-terminal signal peptide for the transport into the periplasm of *C. defragrans*. Replacing the natural tag with the commonly used OmpA-tag (Humphreys et al., 2000; Makrides, 1996) resulted in the fusion protein OmpA-tag-LinD (OL). Initial experiments using cell lysates of *E. coli* JM83(DE3) expressing the genes of OL resulted in the production of 1.2 ± 0.1 mM of compound **3** from 10 mM racemic model substrate **2** after 18 h of biotransformation at 30 °C, representing a 62 % increase in product formation compared to the natural tag. These results are in agreement with the findings of Engleder and colleagues (Engleder et al., 2019), who reported that OL exhibited higher expression levels than native LinD, leading to increased product yields. Further, to confirm the periplasmatic location of LinD and to assess the expression level of LinD wild-type and its variants, mRFP1 was fused C-terminally to OL, resulting in the fusion protein OLm, which enabled the measurement of LinD concentration after chemical lysis of the cells via measurement of fluorescence spectroscopy, and calculation of concentration in relation to IMAC-purified mRFP1 calibration.

The genes of OLm along with other five constructs, (EV, OL, m, Lm, and Om, Table S7) which served as controls, were expressed as described in the supporting information. All six constructs were analyzed macroscopically (Fig. S2) and by fluorescence microscopy to assess the presence or absence of the mRFP1 signal for each construct (Fig. S3). Similar mRFP1 fluorescence levels were observed among the constructs harboring the mRFP1 tag, regardless of whether the tag was located in the cytoplasm or periplasm. This indicates that the cellular localization of the tag did not significantly affect the overall expression level or detectability of the tagged protein, as observed both macroscopically and microscopically (Fig. S2 and S3, respectively). However, the location could still influence the structural conformation and functionality of the protein. To further compare cytoplasmic versus periplasmic localization, the four constructs containing the fluorescent tag were analyzed microscopically at the single-cell level, confirming that OLm is localized in the periplasm of *E. coli* (Fig. S4). These findings highlight the importance of periplasmic expression for achieving higher LinD-catalyzed conversions, likely due to the formation of the disulfide bond between C49 and C102 in the LinD structure, which is promoted by the DsbA-DsbB machinery in the *E. coli* periplasm (Denoncin and Collet, 2013).

To verify the accuracy and reproducibility of our new system OLm, two-phase whole-cell biotransformations with 10 mM racemic model substrate **2** were performed in 10 different biological replicates, each with technical triplicates. This resulted in a coefficient of variation (CV) of 17 % for product formation and 7 % for fluorescence units. Consequently, the normalized enzyme activity, expressed as the quotient of product concentration to fluorescence intensity ([product] fluorescence^{-1}), exhibited a CV of 16 % (Fig. S5). This normalization accounts for variations in protein expression levels, providing a more accurate measure of enzyme activity. Compared to OL, OLm exhibited a 50 % reduction in the formation of **3** from 10 mM racemic **2**, decreasing from 1.0 ± 0.1 mM to 0.5 ± 0.1 mM (Fig. S5), while maintaining comparable reproducibility and enabling quantification of LinD concentration. Notably, initial experiments using cell lysates under single-phase aqueous conditions resulted in a slightly higher product formation of 1.2 ± 0.1 mM, indicating that the activity observed in the two-phase whole-cell system is comparable, albeit moderately reduced. Conversion of 10 mM **4** using the established OLm whole-cell two-phase system resulted in the production of 1.3 ± 0.1 mM of the valuable product **5**. This confirmed the trend previously observed with LinD cell lysate biotransformations (Nestl et al., 2017), namely that **4** yields higher product formation than **2** under identical conditions.

3.2. Active site variants

The postulated mechanism of LinD involves the seven amino acids D39, Y45, M125, H129, C171, C180 and Y240 (Fig. S6) participating in the dehydration and isomerization of linalool through an acid-base mechanism (Cuetos et al., 2020; Nestl et al., 2017). Based on the crystal structure of LinD soaked with geraniol (PDB: 5G1U), residues F40, Y66, and F177 were selected as semi-rational mutagenesis targets, as they are located within ≤ 5 Å of the substrate's hydroxyl group (Fig. S6) and were predicted to influence the conversion of compound **4**. To optimize substrate binding, the active site was modified through point mutations, introducing either bulkier amino acids or alanine, yielding a total of 15 variants. Interestingly, none of the variants showed an increase in product formation compared to the wild-type (Fig. 2). Instead, all tested variants displayed significantly reduced or undetectable activity. Substitutions at position F40 retained the highest residual activity, with F40V reaching 36 ± 3 % of OLm's activity. Variants F40I, F40L, and F40Y also exhibited measurable activity relative to OLm, with 29 ± 9 %, 15 ± 12 %, and 15 ± 5 %, respectively. At the other positions, only Y66F and F177Y showed detectable residual activity, with 10 ± 2 % and 14 ± 3 %, respectively.

These findings further support previous reports that the LinD active site is inherently intolerant to mutation, as most variants exhibited a dramatic loss or complete absence of activity (Cuetos et al., 2020; Wang et al., 2023).

3.3. B-factor analysis and flexible α-helix variants

Due to the limited evolvability of the LinD active site, we focused on the B-factors (Debye, 1912; Sun et al., 2019; Waller, 1923) of the LinD crystal structure (PDB: 5G1W) to identify flexible regions as potential targets for mutagenesis aimed at enhancing the production of compound **5**. This analysis identified a short α-helix comprising the ten residues K103–D112 (Fig. 3) near a previously postulated channel (Weidenweber et al., 2016) as a flexible region (Fig. S7). Within this helix, residues K103, W106, D108, E110, E111, and D112 exhibited significantly higher B-factors compared to the enzyme's average, suggesting their potential role in modulating enzyme activity.

A set of alanine substitution variants for the ten helix residues was generated via QuikChange in OLm and screened. Notably, five of the ten variants showed no detectable formation of **5**, while the remaining five variants exhibited product formation up to 62 ± 4 % compared to the OLm wild-type (Fig. 4, A). As the α-helix residues could be proven to influence conversion of **4**, all ten residues were subjected to saturation mutagenesis by using overlapping extension PCR in combination with the '22c trick' (Kille et al., 2013) to further search for more active variants. Hits were identified by comparing the formation of compound **5** relative to the parental OLm and additionally by analyzing the quotient

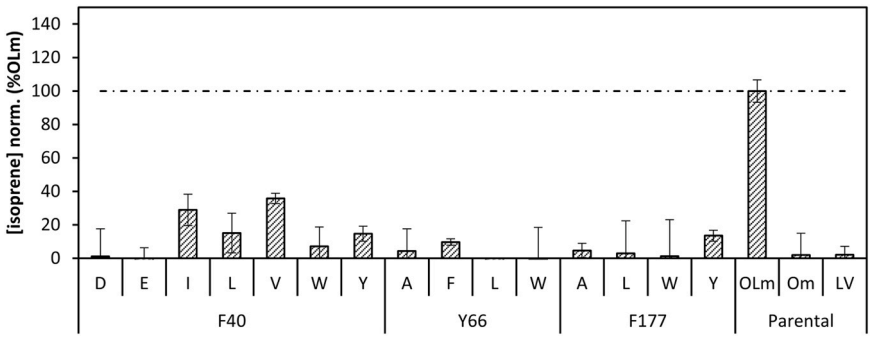

Fig. 2. Product formation of 5 for LinD active site single point variants. Variants were evaluated for their production of 5 from 10 mM 4 (2−3−2), employing the whole-cell two-phase system. As controls, the parental constructs OmpA-LinD-mRFP1 (OLm), OmpA-mRFP1 (Om), and the empty pET-28a(+) vector (EV) were included and treated analogously. Product formation was normalized to the parental construct OLm (100 %, dotted lines). Error bars represent the standard deviation of measurements performed in biological triplicates.

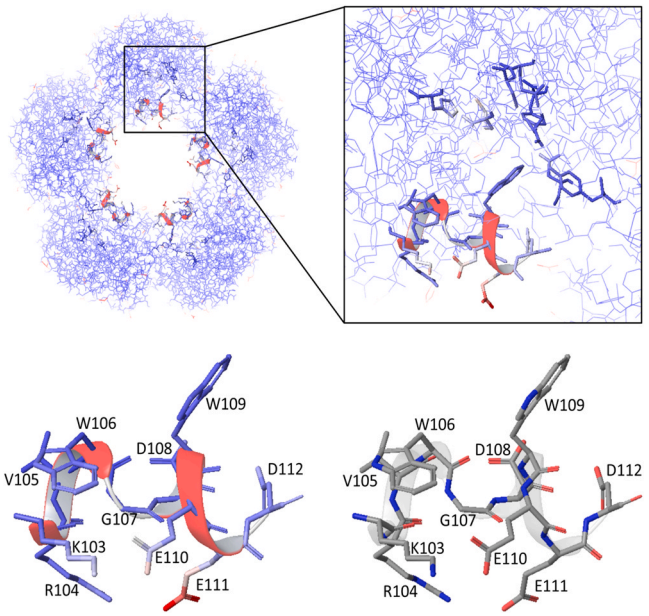

Fig. 3. B-factor analysis of LinD crystal structure in its characteristic pentameric conformation (PDB: 5G1W) depicted by Maestro Version 10.2.010 (Schrödinger K.K.; Tokyo, Japan). High B-factors are depicted in red, low B-factors in blue. Residues of the active site are highlighted in the overall structure (top left), as well as the residues of the identified α-helix showing relatively high B-factors (top right). The respective α-helix consisting of residues K103 to D112 is depicted with (bottom left) and without (bottom right) B-factor color code.

[isoprene] fluorescence^{-1} (Fig. S8) and were confirmed through Sanger sequencing. These variants (K103N, K103R, R104G, G107T, G107D, G107Y, G107V, E110A, E110D, E111G and D112T) were retransformed and expressed in biological triplicates, each accompanied by technical triplicates (Fig. 4, B).

Variants at positions E110 and E111 did not exhibit significant activity enhancements, showing product formation levels comparable to the parental OLm. In contrast, mutations G107T and D112T demonstrated substantial increases in dehydration activity, with enhancements of 208 ± 12 % and 193 ± 6 %, respectively, resulting in the production of 2.8 ± 0.2 mM and 2.6 ± 0.1 mM of product **5**. The obtained fluorescence-normalized values further confirmed the superior performance of these variants, with G107T and D112T exhibiting an increase of 312 ± 16 % and 355 ± 9 % relative to the wild-type enzyme, respectively. Variants K103N and R104G also resulted in notable improvements in product formation, with increases of 173 ± 5 % and 156 ± 12 %, respectively, relative to the parental OLm. However, their fluorescence-normalized values were slightly lower, reaching 152 ± 8 % for K103N and 125 ± 12 % for R104G.

Encouraged by the results of saturation mutagenesis, combinatorial variants comprising mutations K193N, R104G, G107T, and D112T were generated using either QuikChange or overlap extension PCR. Surprisingly, none of the generated double, triple, or quadruple variants exhibited increased product formation compared to the corresponding single-point mutants (Table S8). In fact, nine out of eleven combinatorial variants displayed activities lower than that of the OLm wild-type, indicating negative epistatic interactions between the individually beneficial mutations. These trends were further supported by the fluorescence-normalized values, thereby excluding differences in expression levels as a confounding factor.

Thus, comprehensive kinetic studies were conducted to elucidate the effects of the most promising variants K103N, R104G, G107T, and D112T. To develop a more streamlined approach than the previously reported kinetic analysis of purified LinD (Cuetos et al., 2020), we investigated the feasibility of employing the whole-cell system OLm for kinetic studies. This system facilitates the quantification of total LinD concentration through the fluorescence of the fusion protein.

Preliminary tests, including the evaluation of OLm stability in the two-phase whole-cell setup over a period of up to 120 h during the biotransformation of 10 M provided substrate, showed that the initial activity remained linear for approximately 18 h (data not shown). In addition, under the conditions selected for the kinetic experiments, biotransformation over an 18-hour period resulted in a theoretical conversion below 3 % (Fig. S9). This minimal conversion suggests that the system remained in a steady state throughout the measurement period, thereby justifying the application of the Michaelis-Menten model to determine kinetic parameters. Therefore, we report all kinetic parameters, $K_{m\ (app)}$ and $V_{max\ (app)}$, and $k_{cat\ (app)}$ as apparent values, due to potential uncertainties in the actual substrate concentration available to the enzyme in the aqueous phase caused by substrate partitioning in the two-phase whole-cell system. Notably, data for the G107T variant revealed evidence of substrate inhibition, necessitating appropriate adjustments during data fitting.

Kinetic analyses were conducted for the parental OLm and variants K103R, R104G, G107T, and D112T (Fig. S10). All variants exhibited increased $k_{cat\ (app)}$ values compared to the parental OLm, with G107T and D112T demonstrating 28-fold and fourfold enhancements, respectively (Table 1). Interestingly, the $K_{m\ (app)}$ values varied among the variants: K103N (1.5 mM) was comparable to the parental OLm (0.8 mM), whereas R104G (3.9 mM) and G107T (5.8 mM) showed significant increases, and D112T (0.1 mM) exhibited a notable decrease. For the most active variant G107T, the inhibition constant ($K_{i\ (app)}$) was determined to be 10.0 mM.

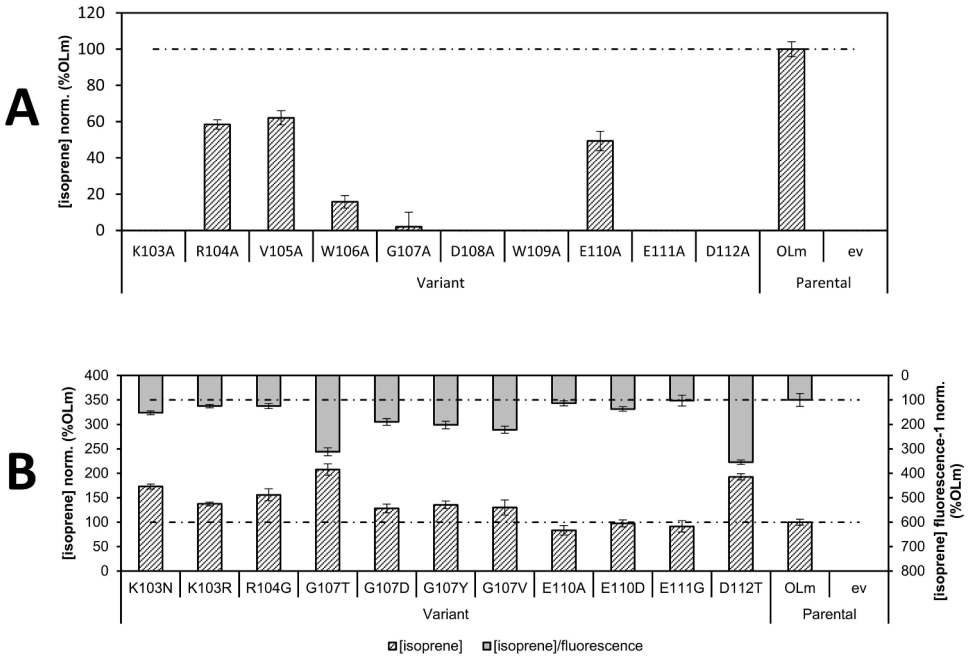

Fig. 4. Product formation of 5 for selected LinD variants of the α-helix residues K103-D112. Variants were evaluated for their production of 5 from 10 mM 4 (2−3−2), employing the whole-cell two-phase system. As controls, the parental constructs OmpA-LinD-mRFP1 (OLm) and the empty pET-28a(+) vector (EV) were included and treated analogously. Product formation was normalized to the parental construct OLm (100 %, dotted lines). A: Alanine-substitution variants of the α-helix residues K103-D112 B: Most active saturation variants of α-helix residues K103-D112. Error bars represent the standard deviation of measurements performed in biological triplicates.

Table 1
Apparent kinetic parameters of OLm wild-type and its variants K103N, R104G, G107T and D112T determined through biotransformations in a whole-cell two-phase system with varying concentrations of substrate 4.

Variant	$K_{m\ (app)}$ (mM)	$K_{i\ (app)}$ (mM)	$V_{max\ (app)}$ (mU)	$k_{cat\ (app)}$ (s^{-1})
K103N	1.5	ND	36.4	42.2
R104G	3.9	ND	51.3	59.6
G107T	5.8	10.0	189.1	862.4
D112T	0.1	ND	14.0	134.6
OLm	0.8	ND	44.7	31.2

ND: not determined

Since the G107T and D112T variants exhibited the highest overall $k_{cat\ (app)}$ values, they were selected for further characterization through crystallization, computational analysis, and molecular dynamics simulations, with the aim of gaining deeper insights into how the introduced mutations impact catalysis. The analysis specifically focused on the movement of the region surrounding the putative substrate channel located within the interior of the cyclic homopentamer of LinD (Weidenweber et al., 2016).

3.4. Crystallography and computational analysis

To shed light on the enhanced activity of the most active variant, G107T, we determined its structure through X-ray crystallography at a resolution of 1.83 Å. Crystallization attempts of the second most active variant, D112T, remained unsuccessful. Consistent with previous structures of LinD variants (Cuetos et al., 2020), G107T displayed five monomers in the asymmetric unit, forming the characteristic toroidal pentamer. Although the variant was co-crystallized with substrate **4** (5 mM), the omit electron density, following protein atom and water molecule building and refinement, was insufficient to model the substrate or its dehydration product **5**. The LinD G107T monomer (PDB: 7AD2) superimposed with the wild-type LinD monomer (PDB: 5G1W) with an RMSD of 0.16 Å over 364Cα atoms, indicating no significant structural changes in monomer structure (Fig. 5).

However, in the active site, the mobile methionine residue M125, known to play a role in catalysis (Cuetos et al., 2020), adopted the 'closed' conformation, with its sulfur atom positioned between the side chains of C180 and H129. At position 107, clear electron density was observed for the new Thr side chain. The Gly to Thr mutation introduced a new hydrogen bond between the threonine hydroxyl group and Glu111, which, in the wild-type enzyme, is exposed to solvent. This interaction caused a slight displacement of the peptide backbone between residues V105 and W109.

3.5. Molecular dynamics simulations

To investigate how the introduced G107T and D112T mutations affect the kinetic parameters of LinD, molecular dynamics (MD)

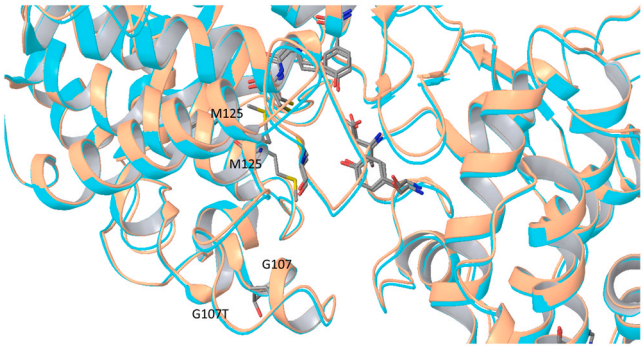

Fig. 5. Structural alignment of the crystal structures of LinD wild-type and variant G107T. LinD wild-type structure (PDB: 5G1W) is shown in orange, G107T variant (PDB: 7AD2) in cyan. The structural alignment was performed using Maestro version 10.2.010 (Schrödinger K.K.; Tokyo, Japan). The flexible residue M125, known to be involved in catalysis, is observed in the 'closed' conformation in the crystal structure of the G107T variant. The residues of the active site are highlighted as well as residues G107 and G107T, respectively.

simulations coupled to substrate access tunnel calculations with CaverDock were conducted (Vavra et al., 2019). MD simulations were initiated from either the corresponding X-ray structure or the *in silico* generated D112T variant model, with an accumulated MD simulation time of 7.5 μs (SI chapter 5). These MD simulations were further analyzed by means of dimensionality reduction techniques, providing insights into the conformational ensemble sampled by wild-type LinD and variants.

The reconstruction of the conformational ensemble of wild-type and G107T indicates that the kinetically most relevant distances contain residues Glu110, Thr116, and Asp117, situated close to G107T point mutation. Both wild-type and variant G107T explore the X-ray-like conformational state 1 (Fig. 6) that presents a main substrate access channel with a bottleneck radius of ca. 1.95 Å (1.95 ± 0.58 Å and 1.91 ± 0.34 Å, respectively). However, variant G107T explores an additional conformation 2 (Conf 2 in Fig. 6), not observed in the case of wild-type, that presents the α-helix (87−111) and loop (113−123) closer to the catalytic residue Asp39. This new conformation promoted by G107T mutation generates an additional substrate access tunnel characterized by a wider bottleneck radius of 2.33 ± 0.24 Å (Fig. 6).

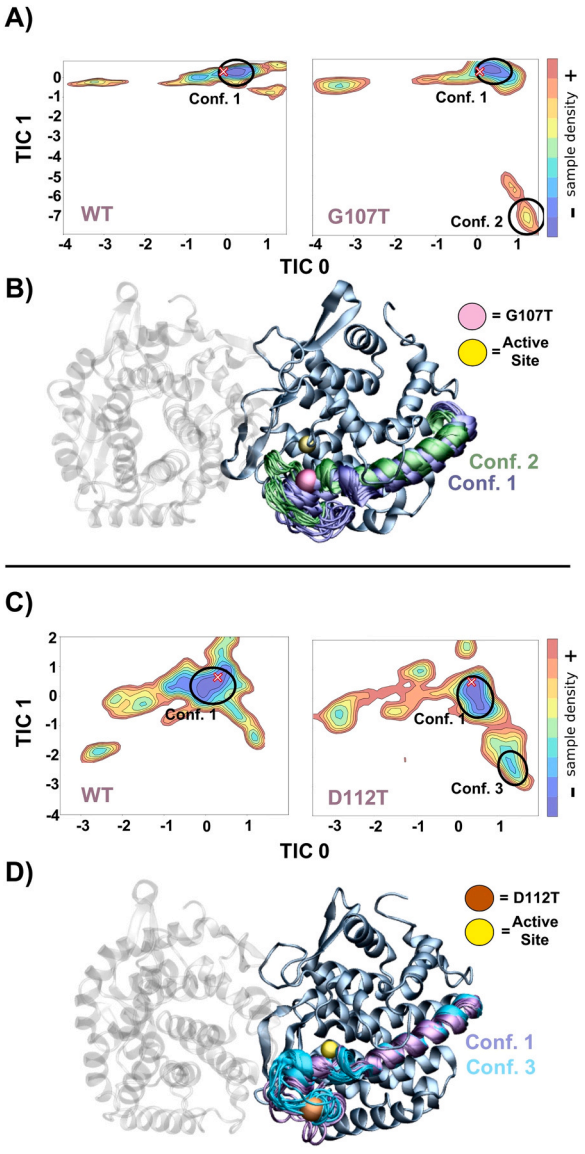

Fig. 6. Conformational population analysis obtained from tICA dimensionality reduction of MD simulation data of WT and G107T (A) and WT and D112T (C) variants. Most populated regions are displayed in blue, whereas less populated in red. Projection of the X-ray structure into the corresponding conformational space is represented with a red cross. Representative ensemble of conformations sampled during the MD simulations are represented as a dimeric LinD structure conforming one catalytic active site (B, D). Protein structure is represented as a cartoon with α-helix conformations coloured in purple for the main energy minima and green, or cyan for alternative conformations. LinD active site location is represented with a yellow sphere. Single point mutations G107T and D112T are shown as a pink or orange sphere, respectively.

A similar behavior is observed for the combined analysis of wild-type and the D112T variant (Fig. 6). In the case of this D112T variant, a new set of conformations is observed, characterized by the movement of Pro118, Ile119, Glu120, and Lys121 residues. Contrary to the G107T variant, this new conformation was also observed for the wild-type enzyme, although to a lesser extent. As observed for conformation 2 in the case of G107T variant, this new conformation 3 is also characterized by a wider bottleneck radius of 2.14 ± 0.52 Å as compared to 1. However, it is slightly narrower than the one identified for the G107T variant (by approximately 0.2 Å). These findings indicate that the introduction of single point mutations in the α-helix or adjacent loop alter their conformational dynamics, thus modifying substrate entry channels and explaining differences in kinetic parameters measured experimentally. Similar observations have been reported for other enzymes, such as the cumene dioxygenase from *Pseudomonas fluorescens* IP01 (Heinemann et al., 2021). In this case, single point mutations in flexible loops near the substrate entrance were sufficient to reshape the substrate tunnel, significantly affecting both enzyme activity and regioselectivity across various substrates.

Substrate accessibility across conformational states 1–3 was further assessed by the calculation of the associated energy barriers for substrate entry and binding to the active site (Fig. 7). For the ensemble of LinD wild-type conformations (Fig. 7, WT Conf. 1), a small energy barrier for substrate entry was identified, in accordance with its narrower tunnel bottleneck radius derived previously, and the lower turnover measured experimentally.

In conformation 2 of the G107T variant, no energetic barrier was detected for substrate entry, which could explain the experimentally observed increase in $k_{cat\ (app)}$ (Fig. 7, G107T Conf. 2). However, this would typically also be expected to lower the $K_{m\ (app)}$, which is not consistent with experimental observations. Since $k_{cat\ (app)}$ is measured under substrate-saturating conditions, energy barriers related to substrate binding should not directly affect it. Instead, the same energetic landscape could influence product release. Therefore, a plausible explanation is that the reaction rate is not limited by the chemical conversion step, but rather by product release. In this scenario, conformation 2 of the G107T variant may facilitate product exit through a smoother energy transition, thus enhancing $k_{cat\ (app)}$. The higher $K_{m\ (app)}$ observed for this variant could result from the altered binding energetics in conformation 2; although there is no entry barrier, substrate binding appears to be less energetically favorable, as illustrated in Fig. 7.

Substrate inhibition, however, is a more complex phenomenon to rationalize. One possible explanation is that the enlarged active site cavity in the G107T variant permits the binding of multiple substrate molecules simultaneously. This could hinder product release either by direct steric blockage or by restricting conformational flexibility, mechanisms that have been previously reported for the haloalkane dehalogenase LinB from *Sphingobium japonicum* UT26 (Kokkonen et al., 2021).

A similar behavior was observed for variant D112T, which also showed no detectable energy barrier for substrate entry (Fig. 7, D112T Conf. 3). However, unlike G107T, the D112T variant exhibits a broad and stable energy minimum near the active site, located approximately 5–8 Å from the catalytic residues, which might explain the substantially more favorable $K_{m\ (app)}$ values obtained experimentally.

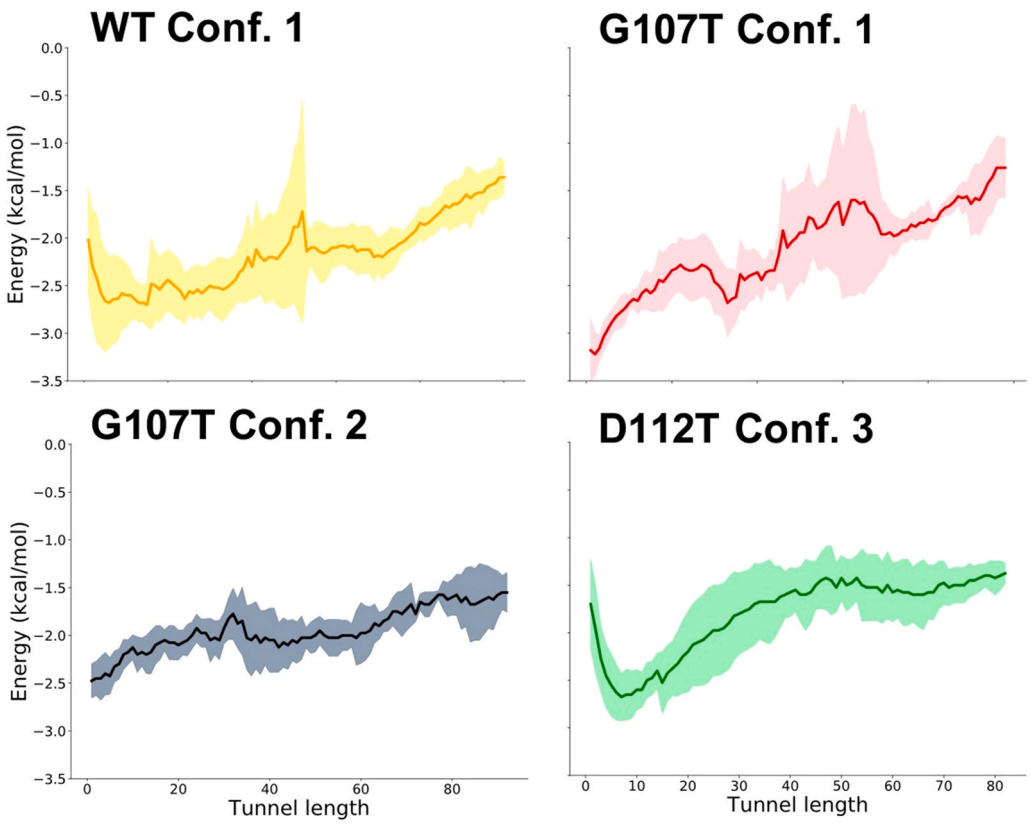

Fig. 7. Estimated transportation energy profiles of substrate 4 for LinD wild-type, variants G107T and D112T computed along the tunnel, transporting the substrate from the active site (at low values of tunnel lengths) to the bulk solvent (higher values of tunnel lengths) for five randomly selected MD snapshots each. The mean energy profile for substrate accessibility to the active site is shown with a solid line, and the standard deviation using a shaded region.

4. Conclusion

This work focused on enhancing the LinD-catalyzed conversion of **4** to the valuable product **5** in a recombinant whole-cell system. To minimize substrate and product loss due to volatility, we established a novel two-phase whole-cell biotransformation setup coupled with a rapid GC method, enabling robust medium-throughput screening. Periplasmic expression of LinD using the OmpA-tag (OL) increased product formation by 62 %. Further, C-terminal fusion with mRFP1 (OLm) allowed direct quantification of enzyme levels and in vivo kinetic analysis.

Using OLm, biotransformations yielded 1.3 ± 0.1 mM **5** from 10 mM **4** within 18 h. To further improve production of **5**, site-saturation mutagenesis targeting a flexible α-helix identified four beneficial variants, K103N, R104G, G107T, and D112T, displaying increased activity of up to 208 % compared to OLm. Kinetic analysis confirmed improved $k_{cat\ (app)}$ values, particularly for G107T and D112T. Computational analyses revealed that structural changes in the α-helix region modulate the substrate access channel, reducing entry barriers and modifying binding energetics. For G107T and D112T, these effects explain the enhanced catalytic turnover observed experimentally. Notably, our energy barrier analysis further indicated that in the most active variants, product release rather than substrate binding likely represents the rate-limiting step, a hypothesis supported by the detection of substrate inhibition in G107T. In biotransformations with 10 mM **4**, the G107T and D112T variants achieved increased product concentrations of 2.8 ± 0.2 mM and 2.6 ± 0.1 mM **5**, respectively.

Our results demonstrate that even minor modifications in regions outside the catalytic center can profoundly impact enzyme performance by influencing substrate and product diffusion. Substrate and product movement through the enzyme were identified as key rate-limiting factors, highlighting critical new targets for further optimization. These insights are consistent with findings in other enzyme families, where conformational changes in access tunnels or loop regions significantly affect activity (Heinemann et al., 2020, 2021; Rapp et al., 2021). This work highlights the value of combining experimental and computational approaches for the rational engineering of enzymes.

CRediT authorship contribution statement

Jan Klenk: Validation, Investigation, Formal analysis, Data curation. **Wendy Escobedo-Hinojosa:** Writing – original draft, Visualization, Validation, Software, Methodology, Investigation, Formal analysis, Data curation, Conceptualization. **Jan Seeger:** Validation, Methodology, Investigation, Data curation. **Bettina M. Nestl:** Supervision, Project administration, Methodology, Formal analysis, Conceptualization. **Gideon Grogan:** Writing – review & editing, Supervision, Resources, Project administration, Methodology, Funding acquisition, Data curation, Conceptualization. **Anibal Cuetos:** Visualization, Validation, Software, Methodology, Investigation, Formal analysis, Data curation. **Sílvia Osuna:** Writing – review & editing, Supervision, Resources, Project administration, Methodology, Funding acquisition, Data curation, Conceptualization. **Javier Iglesias-Fernández:** Visualization, Validation, Software, Methodology, Investigation, Formal analysis, Data curation. **Julian L. Wissner:** Writing – review & editing, Writing – original draft, Visualization, Validation, Formal analysis, Data curation, Conceptualization. **Gloria Saab-Rincón:** Writing – review & editing, Validation, Resources, Formal analysis. **Max-Philipp Fischer:** Writing – original draft, Visualization, Validation, Software, Methodology, Investigation, Formal analysis, Data curation, Conceptualization. **Bernhard Hauer:** Writing – review & editing, Supervision, Resources, Project administration, Funding acquisition, Conceptualization.

Declaration of Competing Interest

The authors declare that they have no known competing financial interests or personal relationships that could have appeared to influence the work reported in this paper.

Acknowledgements

This project has received funding from the European Union's Horizon 2020 Research and Innovation Program under Grant agreement No 635536. Expression strain *E. coli* JM83(DE3) was kindly provided by Sven Panke (ETH Zürich, Basel, Switzerland). A.C. was funded by grant BB/P005578/1 from the BBSRC. We thank Dr. Johan P. Turkenburg and Mr. Sam Hart for assistance with X-ray data collection and the Diamond Light Source for access to beamline I03 under proposal number mx-9948. Special Thanks go to Rebecca Demming and Jens Schmid for fruitful discussions. W.E.H. research work was supported by UNAM-PAPIIT IT201525. J.I.F. and S.O. thank the Generalitat de Catalunya for the emerging group CompBioLab (2017 SGR-1707) and Spanish MINECO for project PGC2018–102192-B-I00. J.I.F. was supported by the European Community for Marie Curie fellowship (H2020-MSCA-IF-2016–753045) and Juan de la Cierva-Incorporación fellowship (IJCI-2017–34129). S.O. is grateful to the funding from the European Research Council (ERC) under the European Union's Horizon 2020 research and innovation program (ERC-2015-StG-679001), and the Human Frontier Science Program (HFSP) for project grant RGP0054/2020.

Appendix A. Supporting information

Supplementary data associated with this article can be found in the online version at doi:10.1016/j.jbiotec.2025.07.019.

Data availability

Data will be made available on request.

References

Brodkorb, D., Gottschall, M., Marmulla, R., Lüddeke, F., Harder, J., 2010. Linalool dehydratase-isomerase, a bifunctional enzyme in the anaerobic degradation of monoterpenes. J. Biol. Chem. 285 (40), 30436–30442. https://doi.org/10.1074/jbc.M109.084244.

Campbell, R.E., Tour, O., Palmer, A.E., Steinbach, P.A., Baird, G.S., Zacharias, D.A., Tsien, R.Y., 2002. A monomeric red fluorescent protein. Proc. Natl. Acad. Sci. 99 (12), 7877–7882. https://doi.org/10.1073/pnas.082243699.

Chauvel, A., & Lefebvre, G. (1989). The Treatment of Olefinic C4 and C5 Cuts. In Petrochemical Processes (Vol. 1). Editions Technips.

Cuetos, A., Iglesias-Fernández, J., Danesh-Azari, H.R., Zukic, E., Dowle, A., Osuna, S., Grogan, G., 2020. Mutational analysis of linalool dehydratase isomerase suggests that alcohol and alkene transformations are catalyzed using noncovalent mechanisms. ACS Catal. 10 (19), 11136–11146. https://doi.org/10.1021/acscatal.0c02958.

Debye, P., 1912. Zur Theorie der spezifischen Wärmen. Ann. Der Phys. 344 (14), 789–839. https://doi.org/10.1002/andp.19123441404.

Demming, R.M., Fischer, M.P., Schmid, J., Hauer, B., 2018. De)hydratases — recent developments and future perspectives. In: Current Opinion in Chemical Biology, 43. Elsevier Ltd, pp. 43–50. https://doi.org/10.1016/j.cbpa.2017.10.030.

Demming, R.M., Hammer, S.C., Nestl, B.M., Gergel, S., Fademrecht, S., Pleiss, J., Hauer, B., 2019. Asymmetric enzymatic hydration of unactivated, aliphatic alkenes. Angew. Chem. 131 (1), 179–183. https://doi.org/10.1002/ange.201810005.

Demming, R.M., Otte, K.B., Nestl, B.M., Hauer, B., 2017. Optimized Reaction Conditions Enable the Hydration of Non-natural Substrates by the Oleate Hydratase from Elizabethkingia meningoseptica. ChemCatChem 9 (5), 758–766. https://doi.org/10.1002/cctc.201601329.

Denoncin, K., Collet, J.F., 2013. Disulfide bond formation in the bacterial periplasm: Major achievements and challenges ahead. In: Antioxidants and Redox Signaling, 19. Mary Ann Liebert Inc, pp. 63–71. https://doi.org/10.1089/ars.2012.4864.

Engleder, M., Müller, M., Kaluzna, I., Mink, D., Schürmann, M., Leitner, E., Pichler, H., Emmerstorfer-Augustin, A., 2019. Exploring castellaniella defragrans linalool (De) hydratase-Isomerase for enzymatic hydration of alkenes. Molecules 24 (11), 2092. https://doi.org/10.3390/molecules24112092.

Engleder, M., Strohmeier, G.A., Weber, H., Steinkellner, G., Leitner, E., Müller, M., Mink, D., Schürmann, M., Gruber, K., Pichler, H., 2019. Weiterentwicklung der substrattoleranz von elizabethkingia meningoseptica oleathydratase zur regio- und stereoselektiven hydratisierung von ölsäurederivaten. Angew. Chem. 131 (22), 7558–7563. https://doi.org/10.1002/ange.201901462.

Frija, L.M.T., Afonso, C.A.M., 2012. Amberlyst ®-15: a reusable heterogeneous catalyst for the dehydration of tertiary alcohols. Tetrahedron 68 (36), 7414–7421. https://doi.org/10.1016/j.tet.2012.06.083.

Gibson, D.G., Young, L., Chuang, R.Y., Venter, J.C., Hutchison, C.A., Smith, H.O., 2009. Enzymatic assembly of DNA molecules up to several hundred kilobases. Nat. Methods 6 (5), 343–345. https://doi.org/10.1038/nmeth.1318.

Härterich, N., Schneider, A., Horz, P., Travnicek, N.D., Hauer, B., 2025. Structure-guided engineering of oleate hydratase for the synthesis of small chiral alcohols without decoy molecule. Adv. Synth. Catal. https://doi.org/10.1002/adsc.202401358.

Heinemann, P.M., Armbruster, D., Hauer, B., 2021. Active-site loop variations adjust activity and selectivity of the cumene dioxygenase. Nat. Commun. 12 (1). https://doi.org/10.1038/s41467-021-21328-8.

Heinemann, P.M., Rapp, L.R., Hauer, B., 2020. Loops und tunnel: unterschätzte elemente in enzymen. BioSpektrum 26 (4), 434–436. https://doi.org/10.1007/s12268-020-1394-2.

Humphreys, D.P., Sehdev, M., Chapman, A.P., Ganesh, R., Smith, B.J., King, L.M., Glover, D.J., Reeks, D.G., Stephens, P.E., 2000. High-level periplasmic expression in Escherichia coli using a eukaryotic signal peptide: Importance of codon usage at the 5' end of the coding sequence. Protein Expr. Purif. 20 (2), 252–264. https://doi.org/10.1006/prep.2000.1286.

Isar, J., Jain, D., Joshi, H., Dhoot, S., Rangaswamy, V., 2022. MICROBIAL isoprene production: an overview. In: World Journal of Microbiology and Biotechnology, 38. Springer Science and Business Media B.V. https://doi.org/10.1007/s11274-022-03306-4.

Isenberg, N., Grdinic, M., 1969. A modern look at Markovnikov's rule and the peroxide effect. J. Chem. Educ. 46 (9), 601. https://doi.org/10.1021/ed046p601.

Kastaniotis, A.J., Autio, K.J., Sormunen, R.T., Hiltunen, J.K., 2004. Htd2p/Yhr067p is a yeast 3-hydroxyacyl-ACP dehydratase essential for mitochondrial function and morphology. Mol. Microbiol. 53 (5), 1407–1421. https://doi.org/10.1111/j.1365-2958.2004.04191.x.

Kille, S., Acevedo-Rocha, C.G., Parra, L.P., Zhang, Z.G., Opperman, D.J., Reetz, M.T., Acevedo, J.P., 2013. Reducing codon redundancy and screening effort of combinatorial protein libraries created by saturation mutagenesis. ACS Synth. Biol. 2 (2), 83–92. https://doi.org/10.1021/sb300037w.

Kokkonen, P., Beier, A., Mazurenko, S., Damborsky, J., Bednar, D., Prokop, Z., 2021. Substrate inhibition by the blockage of product release and its control by tunnel engineering. RSC Chem. Biol. 2 (2), 645–655. https://doi.org/10.1039/D0CB00171F.

Kunkel, T.A., 1985. Rapid and efficient site-specific mutagenesis without phenotypic selection. Proc. Natl. Acad. Sci. 82 (2), 488–492. https://doi.org/10.1073/pnas.82.2.488.

Li, J.X., Smeland, T.E., Schulz, H., 1990. D-3-hydroxyacyl coenzyme A dehydratase from rat liver peroxisomes. Purification and characterization of a novel enzyme necessary for the epimerization of 3-hydroxyacyl-CoA thioesters. J. Biol. Chem. 265 (23), 13629–13634. https://doi.org/10.1016/S0021-9258(18)77395-X.

Makrides, S.C., 1996. Strategies for achieving high-level expression of genes in Escherichia coli. Microbiol. Rev. 60 (3), 512–538. https://doi.org/10.1128/MMBR.60.3.512-538.1996.

Nestl, B.M., Geinitz, C., Popa, S., Rizek, S., Haselbeck, R.J., Stephen, R., Noble, M.A., Fischer, M.P., Ralph, E.C., Hau, H.T., Man, H., Omar, M., Turkenburg, J.P., Van Dien, S., Culler, S.J., Grogan, G., Hauer, B., 2017. Structural and functional insights into asymmetric enzymatic dehydration of alkenols. Nat. Chem. Biol. 13 (3), 275–281. https://doi.org/10.1038/nchembio.2271.

Nestl, B.M., Nebel, B.A., Hauer, B., 2011. Recent progress in industrial biocatalysis. Curr. Opin. Chem. Biol. 15 (2), 187–193. https://doi.org/10.1016/j.cbpa.2010.11.019.

Neufeld, R.J., Peleg, Y., Rokem, J.S., Pines, O., Goldberg, I., 1991. l-Malic acid formation by immobilized Saccharomyces cerevisiae amplified for fumarase. Enzym. Microb. Technol. 13 (12), 991–996. https://doi.org/10.1016/0141-0229(91)90122-Q.

Raju, S., Moret, M.E., Klein Gebbink, R.J.M., 2015. Rhenium-catalyzed dehydration and deoxydehydration of alcohols and polyols: opportunities for the formation of olefins from biomass. ACS Catal. 5 (1), 281–300. https://doi.org/10.1021/cs501511x.

Rapp, L.R., Marques, S.M., Zukic, E., Rowlinson, B., Sharma, M., Grogan, G., Damborsky, J., Hauer, B., 2021. Substrate anchoring and flexibility reduction in CYP153AM.aqLeads to highly improved efficiency toward octanoic acid. ACS Catal. 11 (5), 3182–3189. https://doi.org/10.1021/acscatal.0c05193.

Resch, V., Hanefeld, U., 2015. The selective addition of water. In: Catalysis Science and Technology, 5. Royal Society of Chemistry, pp. 1385–1399. https://doi.org/10.1039/c4cy00692e.

Shoda, S.I., Uyama, H., Kadokawa, J.I., Kimura, S., Kobayashi, S., 2016. Enzymes as green catalysts for precision macromolecular synthesis. Chem. Rev. 116 (4), 2307–2413. https://doi.org/10.1021/acs.chemrev.5b00472.

Sun, Z., Liu, Q., Qu, G., Feng, Y., Reetz, M.T., 2019. Utility of B-factors in protein science: interpreting rigidity, flexibility, and internal motion and engineering thermostability. In: Chemical Reviews, 119. American Chemical Society, pp. 1626–1665. https://doi.org/10.1021/acs.chemrev.8b00290.

Taalman, R.D.F.M., 1996. Isoprene: background and issues. Toxicology 113 (1–3), 242–246. https://doi.org/10.1016/0300-483X(96)03452-X.

Vavra, O., Filipovic, J., Plhak, J., Bednar, D., Marques, S.M., Brezovsky, J., Stourac, J., Matyska, L., Damborsky, J., 2019. CaverDock: a molecular docking-based tool to analyse ligand transport through protein tunnels and channels. Bioinformatics 35 (23), 4986–4993. https://doi.org/10.1093/bioinformatics/btz386.

Waller, I., 1923. Zur Frage der Einwirkung der Wärmebewegung auf die Interferenz von Röntgenstrahlen. Z. F. üR. Phys. 17 (1), 398–408. https://doi.org/10.1007/BF01328696.

Wang, X., Wang, J., Zhang, X., Zhang, J., Zhou, Y., Wang, F., Li, X., 2023. Efficient myrcene production using linalool dehydratase isomerase and rational biochemical process in Escherichia coli. J. Biotechnol. 33–40. https://doi.org/10.1016/j.jbiotec.2023.05.008.

Weidenweber, S., Marmulla, R., Ermler, U., Harder, J., 2016. X-ray structure of linalool dehydratase/isomerase from Castellaniella defragrans reveals enzymatic alkene synthesis. FEBS Lett. 590 (9), 1375–1383. https://doi.org/10.1002/1873-3468.12165.

Yamamoto, K., Tosa, T., Yamashita, K., Chibata, I., 1976. Continuous production ofL-malic acid by immobilizedBrevibacterium ammoniagenes cells. Eur. J. Appl. Microbiol. 3 (3), 169–183. https://doi.org/10.1007/BF01385432.

Zhang, X., Desrochers, S.J., Carl, A.D., Geagea, N., Zielinski, K., Emmert, M.H., 2016. Low temperature dehydrations of non-activated alcohols: Via halide catalysis. Org. Chem. Front. 3 (6), 701–708. https://doi.org/10.1039/c6qo00069j.